Journal of
MATERIALS RESEARCH

Welcome Comments Help

Mutually reactive elements in a glass host matrix: Ag and S ion implantation in silica

R. Bertoncello, S. Gross, and F. Trivillin
I.N.S.T.M. and Dipartimento di Chimica Inorganica, Metallorganica ed Analitica, Università di Padova, via Loredan 4, 35131-Padova, Italy

E. Cattaruzza,[a] G. Mattei, F. Caccavale, and P. Mazzoldi
Istituto Nazionale per la Fisica della Materia (I.N.F.M.) and Dipartimento di Fisica, Università di Padova, via Marzolo 8, 35131-Padova, Italy

G. Battaglin
Istituto Nazionale per la Fisica della Materia (I.N.F.M.) and Dipartimento di Chimica Fisica, Università di Venezia, Dorsoduro 2137, 30123-Venezia, Italy

S. Daolio
Istituto di Polarografia ed Elettrochimica Preparativa-C.N.R., c.so Stati Uniti 4, 35127-Padova, Italy

(Received 29 July 1998; accepted 4 March 1999)

Ag, S, Ag + S, and S + Ag single and double ion implantations in silica glass were performed at room temperature. The implantation energies were chosen in order to get a projected range of 40 nm. The fluences were 2×10^{16} S^+ cm^{-2} and 5×10^{16} Ag^+ cm^{-2}. Silver interacts weakly with the host silica matrix and forms essentially metallic clusters; this weak interaction between Ag and SiO_2 induces formation of silver silicate rather than silver oxide. Double ion implantations of silver and sulfur lead to chemical interaction between the two species that is critically influenced by the implantation sequence. In particular, in the Ag + S sample silver and sulfur atoms react to form crystalline core (Ag)–shell (Ag_2S) nanoclusters.

I. INTRODUCTION

Composite materials as nanosized semiconductor or metal particles embedded in glasses attract much interest as viable candidates for all-optical devices.[1] In particular, metal nanoclusters embedded in glasses can lead to an enhanced third order susceptibility, $\chi^{(3)}$, whose real part is related to the intensity-dependent refractive index.[2–6] There are many different ways to prepare metal or semiconductor doped glasses, namely sol-gel and ion-exchange processes, and processes that use porous glasses. Ion implantation is also a useful tool to produce these (and many other) composite materials: it permits one to pattern the materials, to overcome the doping solubility limits, and to introduce any element in any kind of solid substrate. During irradiation, the interaction between moving ions and substrate determines via radiation damage mechanical stresses, composition, and density modifications; consequently some physical properties of the host glasses, as the optical ones, may change. In addition, it is possible to form new compounds which lead to the formation of regions characterized by very large differences in the refractive index with respect to the substrate.[7–9] The implantation of metal ions is particularly interesting because metal colloids or compounds can be formed, depending on the reactivity of the substrate atoms toward the implanted ones.[10,11] For example, in chromium- and titanium-implanted silica there is formation of silicide and oxide compounds,[12–14] whereas in tungsten-implanted silica the formation of oxides and metallic precipitates takes place.[12] On the other hand, implantation of ion such as gold, silver, lead, copper, and phosphorus leads to the formation of colloids.[6,10,15,16]

In the last few years several papers describing double ion implantations in silica and silicate glasses have been published.[12,16–26] In order to modify both cluster size and cluster chemical composition, if performed sequentially with different atoms the ion implantation extends the possibility of nanostructured system formation and consequently allows one to modulate the physical properties of these composite materials.

In this paper we investigate the chemical and physical modifications induced by both single and double Ag and S implantations in amorphous silica. The aim of double ion implantations is to study the behavior of two mutually reactive elements introduced in a host matrix and to investigate the role, in the final products, of chemical and physical interactions. Silver is a chemically stable element and no strong chemical interaction with silica takes place; it is well known that silver ion implantation leads generally to precipitation of metal nanometric clusters that remain embedded in the silica

[a]Address all correspondence to this author.
e-mail: cattaruzza@padova.infm.it

 © 1999 Materials Research Society

Downloaded from https://www.cambridge.org/core. UNIV.STUDI PADOVA-BIBL.RUGGERO, on 05 Mar 2018 at 10:44:56, subject to the Cambridge Core terms of use, available at https://www.cambridge.org/core/terms. https://doi.org/10.1557/JMR.1999.0329

network.[6,10,25] The chemical behavior of sulfur in silica is less predictable, since both elemental sulfur and silicon sulfide are thermodynamically stable species. The most common form of sulfur is S_8, but other oligomers as S_5, S_6, and S_7 (besides the gaseous molecule S_2) are well known too. Since sulfur chemical bond lengths and angles are highly variable, sulfur oligomers are expected to easily locate in the silica network. Alternatively, chemical reaction involving sulfur atoms and the silica substrate can take place. An oxygen atom substitution by a sulfur one should lead to a thiosilicate species; it is worth remembering that the two atoms are isoelectronic. Thus, even if their ionic radii are quite different (S^{2-}: 184 pm, O^{2-}: 140 pm), this substitution is a reasonable possibility.

Chemical affinity of silver with sulfur is well-known: the two species interact to give preferentially silver sulfide, a chemically stable semiconductor compound. As well as silver sulfide, reactions between the two implanted ions and the silica matrix could lead to silicate, thiosilicate, and sulfate species formation. In some of our previous papers[11–16,24,25] we investigated the chemical interactions in ion implanted silica (Ar^+, N^+, Ag^+, Cu^+, W^+, Ti^+, Cr^+, Pt^+) and we evidenced the important role of the chemical driving force in determining the final products. In order to evaluate the influence of the implantation sequence on the silver-sulfur interactions, the double implants have been performed in both sequences; the implantation energies have been chosen to achieve a close in-depth distribution. Further, the investigation of double implantations of different pairs of elements[12,16,24,25] pointed out that final products are determined not only by mutual chemical reactivity of the dopants but also by their interaction with the glass substrate.[16] In order to achieve a deeper knowledge of how and why the final compounds form, a great ensemble of different chemical and physical investigation techniques has been used. This approach becomes necessary if one wants to achieve a deep insight of the interactions that originate in very complex composite materials.

II. EXPERIMENTAL

Herasil I silica samples (supplied by Heraeus) were implanted with S, Ag (single irradiations), S + Ag, and Ag + S ions (double irradiations); "Ag + S" means that the "Ag" implantation is followed by the "S" one. The implants were performed at room temperature. The implantation energies have been chosen in order to get the ion projected range, R_p, of 40 nm for all the implants (30 keV for S, 65 keV for Ag). The values of the ion projected range R_p have been calculated for silica using the TRIM code.[27] The fluences were 2×10^{16} S^+ cm^{-2} and 5×10^{16} Ag^+ cm^{-2} (their ratio approximates the stoichiometric atomic ratio in silver sulfide, Ag_2S), and the ion current densities were $\leqslant 1.5$ μA cm^{-2} for all the implants.

X-ray photoelectron spectroscopy (XPS) and x-ray-excited Auger electron spectroscopy (XE-AES) measurements were achieved with a VG Escalab MK II spectrometer, using nonmonochromatized Mg K_α radiation (1253.6 eV) at a working pressure lower than 10^{-7} Pa. The spectrometer, which uses a five channeltron concentric hemispherical analyzer operating in the constant analyzer energy mode, was previously calibrated assuming the binding energy (B.E.) of $Ag3d_{5/2}$ line for metallic silver at 368.2 eV with respect to the Fermi level. The experimental error in the energy values of the XPS and XE-AES lines is 0.1 eV. Owing to surface charging, samples showed a shift of signal energies of 3–5 eV toward higher binding energies. As internal reference for charging effects we assumed the $O1s$ peak of fused silica to be at 532.7 eV of B.E. Spectra were analyzed with a Shirley-type background subtraction[28] and were fitted using a non-linear least-square fitting program adopting Gaussian–Lorentzian peak shapes. The atomic composition was evaluated using sensitivity factors as determined from theoretical photoionization cross sections and asymmetry parameters, calculated within the Hartree–Fock–Slater one-electron central potential model.[29] XPS and XE-AES depth profiles of the different elements were carried out performing cycles of argon ion sputtering with 3 kV of accelerating potential; in these conditions the sputtering rate was a few tenths of nanometer per minute. All over the depth profiles there was no indication of preferential sputtering induced by Ar^+ etching. The $O1s$ peak shape did not show any asymmetry and $Si2p$ B.E. values always indicated the presence of stoichiometric silica.

Transmission electron microscopy (TEM) analyses were performed with a Philips CM30 microscope operating at 300 kV and equipped with an energy dispersive spectroscopic x-ray microanalyzer (at LAMEL Institute, CNR-Bologna). Cross-sectional samples were prepared by mechanical prethinning followed by a low-angle milling using argon ions with energies of 5 keV. To minimize ion damage, samples were cryogenically cooled during the ion milling process.

Secondary ion mass spectrometry (indicated as SIMS I) measurements were recorded with a CAMECA ims-4f ion microscope equipped with a normal incidence electron gun for charge compensation. Concentration depth profiles were obtained by 14.5 keV Cs^+ bombardment, and by negative-ion detection.

Further SIMS measurements (indicated as SIMS II), mainly dedicated to the analysis of different ion fragments obtained during sample erosion, were performed using a custom-built instrument. A monochromatic (2 keV) ${O_2}^+$ ion beam (collimated to 50 μm) was gen-

Downloaded from https://www.cambridge.org/core. UNIV.STUDI PADOVA-BIBL.RUGGERO, on 05 Mar 2018 at 10:44:56, subject to the Cambridge Core terms of use, available at https://www.cambridge.org/core/terms. https://doi.org/10.1557/JMR.1999.0329

erated in a mass-filtered duoplasmatron ion gun (model DP50B, VG Fisons). The secondary ion optics were of the three-lens design with a central stop interfaced with a Balzers, model QMA 400, quadrupole mass analyzer (mass range extended to $m/z = 2048$). A secondary electron multiplier (90° off-axis) was used for negative- and positive-ion detection in the counting mode. The analysis was carried out with an ion current of the primary beam ranged between 400 and 800 nA.

Rutherford backscattering spectrometry (RBS) analyses were performed using a 2.2 MeV, $^4He^+$ beam and the scattering angle of 160°. In order to enhance the depth profile scale, spectra were recorded with an angle of 55° between the beam direction and the sample normal.

Optical absorption spectra were determined in the 200–800 nm wavelength region by using a CARY 5E UV-VIS-NIR dual-beam spectrophotometer.

Atomic force microscopy (AFM) images were collected using a Park Scientific Autoprobe CP instrument. Images were obtained in contact mode (the force being around 1–2 nN) in air at room temperature, with a scan rate of 0.5 lines s^{-1}. The cantilever used was a Park Scientific Instruments microlever 0.6 μm: a gold-coated silicon nitride cantilever with sharpened tip. The sampled area was 1×1 μm^2. The background was subtracted from the images by using the ProScan 1.3 software from Park Scientific.

III. RESULTS AND DISCUSSION

For the two single implants, RBS measurements show that about 100% (S) and 85% (Ag) of the implantation dose is retained in the silica matrix. In the S-implanted sample, the subsequent silver implantation (S + Ag) induces a sulfur depletion: the S retained dose is now about 50% of the nominal implantation dose (the Ag retained dose is about 90%). In the same way, the sulfur implantation in the previously Ag-implanted silica (Ag + S) causes silver depletion: the Ag retained dose is now about 60% of the implantation dose (100% for S). The depletion of the preimplanted atoms takes place via radiation-enhanced diffusion (RED): host atoms move toward the surface where they are preferentially sputtered. This is a characteristic behavior of chemical elements that react weakly (or do not react at all) with the host silica matrix: (see, e.g., Refs. 24 and 25). This is well known for silver, when the formation of metallic nanoparticles is achieved, and it suggests that chemical reactions between implanted atoms and host ones are, if present, very weak in the case of sulfur, too.

SIMS I measurements confirm this picture. In Fig. 1 we report the Ag sputtering yield of the three Ag-implanted samples. The Ag depth distributions always show a bimodal shape (usually a bimodal distribution

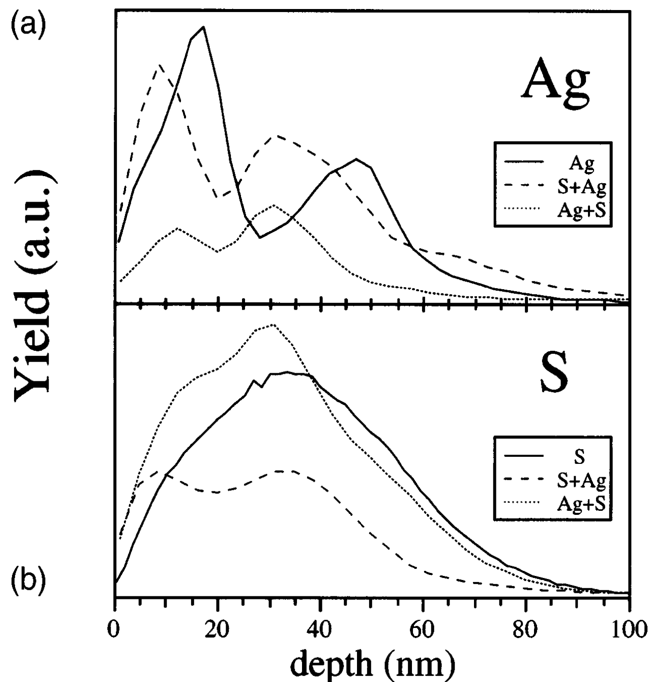

FIG. 1. SIMS I depth profiles of (a) silver and (b) sulfur in the four implanted samples.

is correlated to metallic nanoparticle presence[6,10,25]). In both the double implants (Ag + S, S + Ag), the Ag bimodal depth profile appears shifted toward the surface, which can be due to the well-known mobility of silver in silica matrix. The relative intensities of all the SIMS I spectra are in good agreement with RBS quantitative analyses. In Fig. 1 we also report the sulfur sputtering yield. In the S-implanted silica the shape of the sulfur depth profile is approximately Gaussian; after Ag^+ implantation (S + Ag) the sulfur shows a bimodal distribution that follows the silver depth profile in the same sample. Also in the Ag + S sample it is possible to observe (even if less marked) a correlation between the two depth profiles. The correlation between S and Ag depth profiles can be attributed to two different kinds of phenomena. The first component of the S bimodal distribution might be caused by the presence of chemical driving forces between S and Ag atoms as well as S atoms and substrate defects in a highly damaged region. Sulfur atoms are induced by RED to move toward the surface; some of them follow silver distribution because of chemical driving forces. The second component might be ascribed to the typical depth profile of implanted sulfur; its maximum is positioned very close to that we find in the sulfur single implantation.

Bright-field TEM planar micrographs of the double-irradiated samples are reported in Fig. 2. In both samples we detect the formation of a very large number of nanoparticles embedded in the silica matrix. In the S + Ag sample we find a cluster diameter distribution

Downloaded from https://www.cambridge.org/core. UNIV.STUDI PADOVA-BIBL.RUGGERO, on 05 Mar 2018 at 10:44:56, subject to the Cambridge Core terms of use, available at https://www.cambridge.org/core/terms. https://doi.org/10.1557/JMR.1999.0329

characterized by a mean value of 12 nm and a standard deviation of 5 nm; in the Ag + S one we find 9 and 5 nm, respectively. There are many more particles in the S + Ag double-implanted silica than in the Ag + S one, in agreement with the larger silver content revealed in the S + Ag sample by quantitative RBS analysis. Selected area diffraction patterns (insets of Fig. 2) indicate that in the S+ Ag sample nanoparticles are composed of silver atoms and have the same fcc crystalline structure of the silver bulk phase. In the Ag + S sample, however, the diffraction pattern shows in addition (less intense) spotty rings characteristic of acanthite, one of the three crystalline phases of Ag_2S between the room temperature and the melting point. The formation of acanthite, i.e., the (bulk) Ag_2S stable phase at temperatures lower than about 180 °C, is in agreement with the picture of the ion implantation as a low-temperature physical process,[11,12,14] if regarded at the time scale characteristic of the thermodynamic and diffusive behaviors. Bright-field TEM cross-sectional micrographs of the same samples are reported in Fig. 3. In the S + Ag sample, the in-depth cluster distribution shows a bimodal shape,

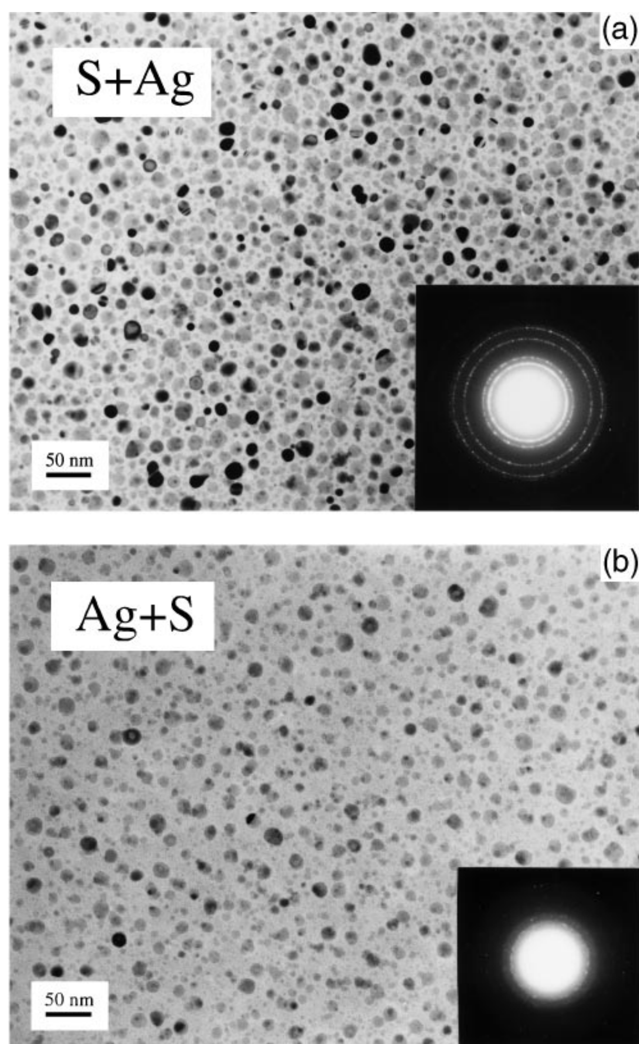

FIG. 2. Bright-field TEM planar micrographs of the (a) S + Ag and the (b) Ag + S implanted silica samples. The insets show the selected area diffraction pattern.

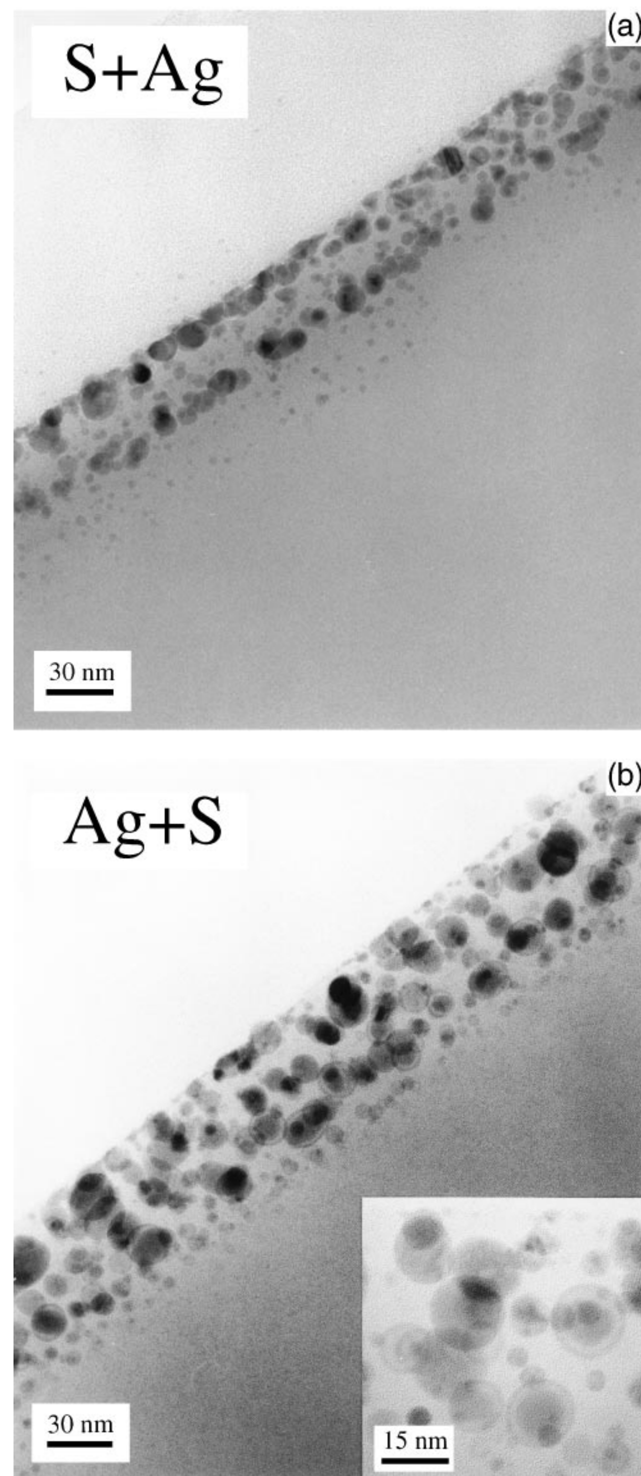

FIG. 3. Bright-field TEM cross-sectional micrographs of the (a) S + Ag and the (b) Ag + S implanted silica samples. The inset shows a high resolution detail of the core-shell clusters.

Downloaded from https://www.cambridge.org/core. UNIV.STUDI PADOVA-BIBL.RUGGERO, on 05 Mar 2018 at 10:44:56, subject to the Cambridge Core terms of use, available at https://www.cambridge.org/core/terms. https://doi.org/10.1557/JMR.1999.0329

in good agreement with the silver depth profile obtained by SIMS I. The largest clusters (diameter ⩾10 nm) are mainly localized at the surface and at 35 nm depth. In the Ag + S sample, the in-depth distribution of cluster dimension is more regular. Here, the (less marked) bimodal shape of the silver depth profile exhibited by SIMS I can be explained by the presence of very small silver nanoparticles (diameter <1 nm) and dispersed silver atoms (i.e., not forming nanoaggregates), both undetectable by TEM. The more regular dimension of nanoparticles can be attributed to the marked RED of silver atoms during the sulfur irradiation. The irradiation-induced defects act as nucleation centers for the diffusing silver atoms, leading to the formation of large silver nanoprecipitates in all the irradiated region.[30] The cross-sectional micrograph of the Ag + S sample clearly shows that many clusters are characterized by a shell structure (see inset of Fig. 3). Given all the previous evidence, it is reasonable to assume these nanoparticles as metallic silver cores surrounded by silver sulfide crystalline shells. These so-called crystalline core-shell clusters (heterosystems) originate only in the deeper implanted regions of the Ag + S sample, where there is a high atomic fraction of sulfur if compared to silver. All these findings suggest that the implantation sequence can be a very important parameter, in order to obtain particular compounds and/or nanostructures by means of double ion implantation.

Optical absorption measurements are reported in Fig. 4. The framework of Maxwell-Garnett[31] and Mie[32] theories explains the absorption band around 400–420 nm[25,33–35] of wavelength as originated by spherical silver nanoparticles, with diameter smaller than about 10 nm, embedded in silica matrix; this is the absorption resonance known as the surface plasmon resonance (SPR). In our Ag-implanted silica sample, the broad absorption band is clearly a superposition of two different signals, with their maximum values centered at about 415 and 490 nm. In the S + Ag sample, the absorption spectrum still shows the high wavelength component while the low one is present only as a weak shoulder. In the Ag + S sample, it seems to be only one absorption peak, centered at about 450 nm.

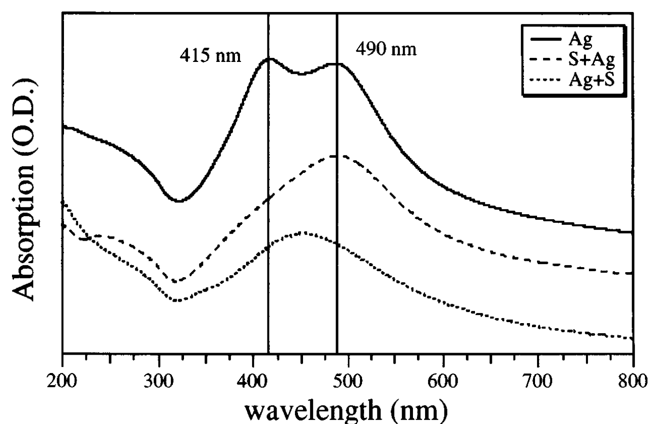

FIG. 4. Optical absorption spectra of the Ag-implanted samples.

The appearance of absorption peaks at different wavelengths can be due to the presence of nanoparticles with different dimensions,[36,37] as observed in silica samples implanted at 300 keV, with 7.6×10^{16} Ag^{+} cm^{-2}.[38] There, the optical absorption shows two distinct bands (centered at 400 and 520 nm) due to the presence of silver nanocluster characterized by two very different sizes (<10 nm and about 50 nm diameter, respectively, as determined by using the peak wavelength dependence of the colloid diameter in the Mie theory[34]; 6 and 40 nm diameter, measured by TEM). In fact, for nanocluster diameters larger than a few nanometers, spectral position λ of the absorption maximum is an increasing function of nanoparticle dimension.[34,35] Moreover, the presence of nonspherical particles may cause optical effects that complicate the absorption spectra. For example, in the case of prolate particles and nonpolarized incident radiation,[39] two broad bands arise because of the different optical absorption between parallel and perpendicular radiation polarization axes with respect to the ellipsoidal particle major one. Finally, for large particles, electric-multipole (i.e., higher than dipole) interactions can cause absorption at larger wavelength.[35] Mutual interactions among closely spaced nanoparticles may also induce several components in absorption spectra.[40]

As far as the double implants are concerned, the SPR absorption peak position may be shifted because of the formation of the core-shell clusters as well as because of the substrate optical properties modification (substrate effects).[16,35,41] It has been recently demonstrated for Au_2S (core)–Au (shell) particles in aqueous medium[42] that a significant red shift of the absorption band takes place. In our samples the formation of these particular structures happens as a consequence of pre- and post-irradiation of the composite material (silver nanoparticles buried in silica) with a reactive element. Sulfur atoms can chemically react with the host matrix atoms as well as with the silver ones. In the latter case reaction may occur with silver atoms that lie on the surface of nanoclusters [Ag (core)–Ag_xS (shell) particles]. As already discussed, the Ag + S sample shows the presence of Ag (core)–Ag_2S (shell) crystalline nanoclusters. However, the hypothesis that S atoms may diffuse inside the Ag cluster to form an Ag_xS (core)–Ag (shell) system cannot be completely rejected.

In order to clarify the chemical role played by sulfur atoms, we have performed further SIMS measurements (indicated as SIMS II) dedicated to the analysis of ion fragments. Our aim was to pick up the presence of Ag–S bonds by analyzing the in-depth ion fragment

Downloaded from https://www.cambridge.org/core. UNIV.STUDI PADOVA-BIBL.RUGGERO, on 05 Mar 2018 at 10:44:56, subject to the Cambridge Core terms of use, available at https://www.cambridge.org/core/terms. https://doi.org/10.1557/JMR.1999.0329

distribution. In all three silver-implanted samples, the considerable presence of Ag^+, $Ag_2{}^+$, and $Ag_3{}^+$ ion fragments agrees with the formation of metallic silver nanoclusters in the silica matrix. In these samples the analysis shows a weak $AgSiO^+$ signal, too. Because of the absence of AgO^+ signal related to the presence of silver oxide, the formation of a small amount of silver silicate takes place. In the doubly implanted samples the SIMS II analysis reveals the presence of Ag_nS^+, ($n = 1, 2, 3$) ion fragments; in the S + Ag sample they are mainly localized on the outermost layers.

In all three sulfur-implanted samples, the absence of any detectable $S_n{}^+$ fragment ($n \geqslant 2$) seems to exclude the formation of –S–S– catenation inside the matrix, even if the presence of S_n species cannot be completely ruled out because the sulfur ion fragments have a very low ionic yield. The detection of a low-intensity SiS^+ fragment signal suggests the presence of a small amount of thiosilicate species in which an oxygen atom of the silica tetrahedron should be substituted by a sulfur atom.

XPS and XE-AES measurements of the three silver-implanted samples show the presence of metallic silver atoms along the whole depth profiles. Because of the low sensibility of the Ag3*d* B.E. position for very different Ag oxidation states,[43–45] the metallic silver presence is evidenced principally by the value of the silver α parameter, i.e., the sum of B.E. of $Ag3d_{5/2}$ and kinetic energy (K.E.) of AgMNN Auger peaks. We find in all three samples that the α_1 value is 726.1 ± 0.3 eV (AgM_4NN) and the α_2 value is 720.8 ± 0.3 eV (AgM_5NN). Typical α parameter values for metallic silver are, respectively, 726.3 ± 0.2 eV and 720.5 ± 0.2 eV, according to literature values[43–45] and to those obtained by performing analyses on a metallic silver plate. For an Ag_2O standard sample we measured $\alpha_1 = 724.3 \pm 0.2$ eV and $\alpha_2 = 718.9 \pm 0.2$ eV and for an Ag_2S sample we found $\alpha_1 = 725.3 \pm 0.2$ eV and $\alpha_2 = 719.3 \pm 0.2$ eV. Shape and K.E. position of AgMNN Auger band seem to indicate the absence of chemical interactions between silver and oxygen and/or sulfur atoms: however, the difficulty to resolve underlying structures in a signal as complex as the AgMNN is, can easily lead to wrong conclusions. From the analysis of this signal we can affirm that, if present, chemical bonds involve only a lesser fraction of the silver atoms.

The O1*s* signal confirmed the absence of silver oxide compounds. As far as sulfur is concerned, XPS data for the three samples implanted with sulfur indicate a zero valent oxidation state at almost all depths. In fact, S2*p* binding energy values, found in the range 163.6–164.6 eV, are very close to that reported in literature, 164.0 eV, for elemental sulfur. Also the values of S2*s* peaks, close to the literature value of 228.0 eV, suggest the presence of elemental sulfur. On the other hand, if the formation of thiosilicate species takes place as suggested from SIMS II results (through the substitution of an oxygen atom of the silica tetrahedron by a sulfur atom), we presume we will detect binding energy values of the sulfur peaks very close to those of elemental sulfur: thiosilicate sulfur undergoes an electronic depletion caused by the proximity of three strongly electronegative oxygen atoms. We have not found XPS literature data of the binding energy of S2*p* peak in thiosilicate species. The TEM evidence of the formation of crystalline Ag_2S in the deeper implanted region of the Ag + S sample does not contradict XPS results. In fact, only a small fraction of silver atoms forms in the crystalline silver sulfide shell of metallic cluster. If we consider the stoichiometry of this compound, it is easy to understand that, even for sulfur atoms, only a small fraction (below the XPS detection limit) of them constitutes silver sulfide.

A different behavior in the XPS sulfur peaks is exhibited by the outermost atomic layers of the S + Ag sample, where the S2*p* signal shows B.E. values (about 162.0 eV) characteristic of sulfide species (Fig. 5). Moving inside the sample, S2*p* binding energy values become closer to elemental sulfur values, as previously described. Hence, the formation of (amorphous) silver sulfide seems to be favored when sulfur is implanted before silver. This evidence is in agreement with SIMS II depth profile of SiS^+ and S^+ ion fragments; in the first layers of the S + Ag sample their yield is low. In correspondence to the same zone, Ag_nS^+ yield shows a maximum. It is reasonable to suppose that during the high fluence Ag irradiation, most of the preimplanted sulfur leaving the sample via RED is formed by atoms that did not react with the matrix. Further, during Ag implantation the silver atoms are principally in the atomic form, i.e., not in the cluster one, favoring in this way chemical interactions with the preimplanted sulfur atoms. Therefore, the percentage of retained sulfur atoms

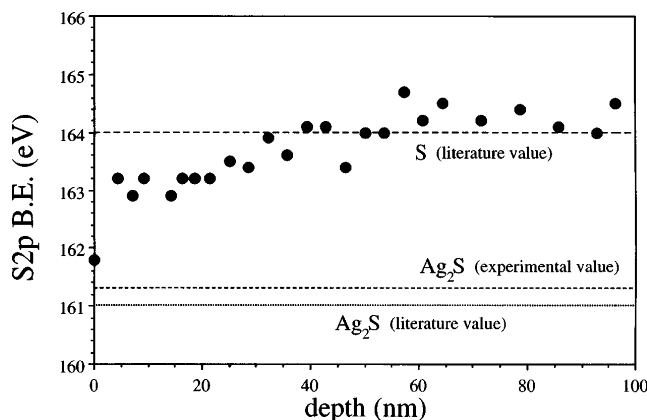

FIG. 5. Binding energy value (•) of the XPS S2*p* peak along the depth profile of the S + Ag implanted sample. Reference values are also displayed.

Downloaded from https://www.cambridge.org/core. UNIV.STUDI PADOVA-BIBL.RUGGERO, on 05 Mar 2018 at 10:44:56, subject to the Cambridge Core terms of use, available at https://www.cambridge.org/core/terms. https://doi.org/10.1557/JMR.1999.0329

that react with the silver ones may be significant in this region. However, the TEM cross-sectional micrograph of the S + Ag sample (Fig. 3) clearly shows that many large clusters were exposed to air contamination, so the well-known mechanism of metallic silver sulfidation due to atmosphere exposure cannot be ruled out. In the Ag + S sample sulfur is implanted after silver; i.e., it penetrates into a composite material formed by Ag clusters embedded in silica. In this case chemical reactions from silver would come from the surface of the metallic clusters and/or a few dispersed atoms.

In all four samples, analyses of the Si2*p* peak (B.E. = 103.6 ± 0.1 eV), of the Si KLL Auger peak (K.E. = 1608.0 ± 0.3 eV), and of the silicon α parameter show[46] that there is no modification of substrate stiochiometry (SiO_2) as a consequence of implantations; this is also confirmed by the intensity quantitative ratio of O1*s* to Si2*p* signals.

In order to get further information on the different modifications induced by the various implants, a morphological investigation of the sample surface has been accomplished by AFM analysis. In order to test the homogeneity of the implanted surface, several images relative to different areas of the sample have been acquired. The images relative to the Ag (not reported) and Ag + S (Fig. 6) implants exhibit a similar surface morphology, characterized by the presence of 60–70 nm diameter features. This morphological similarity demonstrates that the subsequent introduction of sulfur atoms induces no remarkable modification on the previously Ag-implanted surface. On the other hand, the S + Ag (Fig. 6) implanted sample shows a completely different morphology. The granulometry is finer and the diameter of the granules ranges from 20 to 40 nm. An explanation of this different behavior can be found if we consider the effect of the ion introduction sequence. In the S + Ag implanted sample silver is introduced in a matrix where the sulfur is already present. The driving force represented by the chemical affinity between silver and sulfur probably determines a more uniform lateral distribution of Ag at the sample surface. Here a non-negligible amount of silver reacts with sulfur, instead to form metallic nanoclusters (as clearly evidenced by XPS sulfur signals). As a consequence, a finer granulometry of the surface ensues.

The surface of the sulfur single implanted sample appears flat and only slightly damaged. Different morphological modifications between the two single implants could be attributed to differences in implantation dose, energy, and in atomic weight well as to the different reactivity of the two species.

A further support to this hypothesis comes from a detailed analysis of SIMS II depth profile relative to silicon, oxygen, alkali, and contamination metals. In sulfur single implant, silicon, oxygen, and their related fragments show flat profiles. This evidence can be rationalized assuming that silica has not undergone any appreciable modification. In the same implant, signals relative to contamination (a few ppm) metals as Na, K. Ca, Mg, and Al show a maximum of concentration very close to the surface and decrease slowly, moving in depth along the profile. This situation is slightly different in a silver single implant, where maxima relative to contamination metals lie deeper in respect to the first layers of the surface. In principle, this difference could be ascribed to the different doses and energies used, besides different atomic weight between silver and sulfur; all these factors contribute to cause different modifications of the host matrix. A comparison between the double implants points out how, in the S + Ag double implant, the modification induced is higher than in the Ag + S implant. SIMS II depth profiles of the impurities undergo appreciable modifications, and their maxima are located deeper in double implants than in single ones.

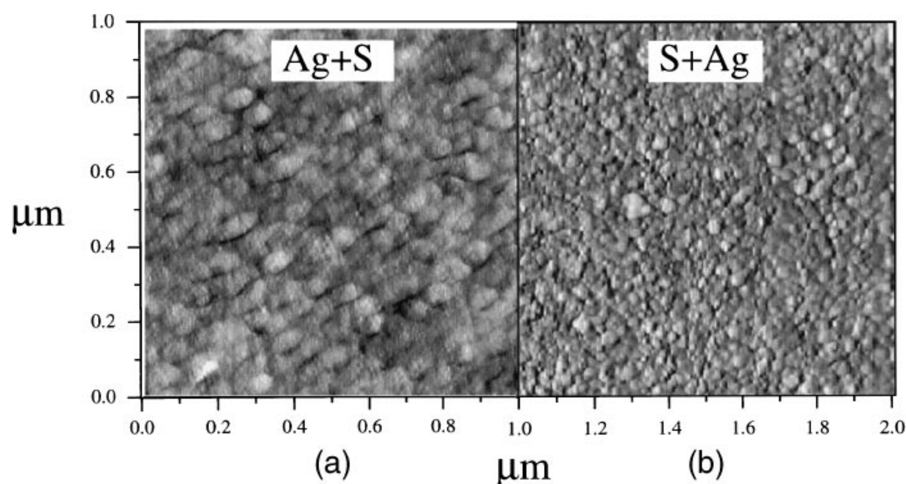

FIG. 6. AFM image of the (a) Ag + S and the (b) S + Ag implanted silica samples.

Downloaded from https://www.cambridge.org/core. UNIV.STUDI PADOVA-BIBL.RUGGERO, on 05 Mar 2018 at 10:44:56, subject to the Cambridge Core terms of use, available at https://www.cambridge.org/core/terms. https://doi.org/10.1557/JMR.1999.0329

These modifications are more evident in the S + Ag double implant than in the Ag + S implant. Implantation sequence seems to play a specific role in determining the damage of the outermost implanted layers.

From the SIMS, TEM, XPS, and XE-AES analyses it turns out that only a modest chemical reactivity occurs between Ag and S atoms. Because the optical absorption band of the Ag + S sample can be fitted in an effective way by two different components (still centered at about 410 and 490 nm), it would be reasonable to assume that the differences among the absorption bands of the three Ag-implanted samples arise principally as a consequence of the different concentrations and dimension distributions of silver nanoclusters. On the other hand, the formation of core-shell clusters can originate from absorption bands whose intensity and wavelength position are very difficult to foresee. Work is in progress to understand the plasmon response of metal nanoparticles surrounded by a shell made of a different compound.

IV. CONCLUSIONS

Ion implantation is a useful tool to produce composite materials. Further, double implantations allow exploitation of the chemical affinity of the two dopant elements in order to obtain nanostructured compounds and/or heterosystems, such as core-shell clusters. In the case of silver and sulfur double implantations, the information collected by the integrated use of complementary techniques allows us to draw the following conclusions: (1) Silver interacts weakly with the host matrix and forms metal clusters, confirming its notable mobility in a silica matrix. The faint interaction with silica is observed to induce the formation of silver silicate species rather than silver oxide species. (2) Sulfur, too, interacts weakly with the host matrix, with the formation of a small quantity of thiosilicate. (3) Sequential ion implantation of silver and sulfur leads to a (moderate) chemical interaction between the two elements. As a matter of fact, the reactivity of the dopant element (Ag or S) is ruled by the presence or by the absence of the other dopant element. The Ag–S chemical interaction is influenced by the implantation sequence: in the S + Ag sample the interaction between sulfur and silver is slightly higher than in the Ag + S sample, even if only in the latter sample we detect the formation of a crystalline phase (acanthite) of Ag_2S. (4) Chemical and morphological modifications of the sample surface are influenced by the implantation sequence.

ACKNOWLEDGMENTS

We are grateful to Professor E. Tondello, director of the Centro di Studio sulla Stabilità e Reattività dei Composti di Coordinazione, CNR-Padova, for the use of the XPS facilities and for helpful discussions. This work was partially supported by Italian MURST (Coordinated Project) and C.N.R.

REFERENCES

1. T. Kobayashi, Nonlinear Opt. **1**, 91 (1991).
2. E.M. Vogel, J. Am. Ceram. Soc. **72**, 719 (1989).
3. F. Hache, D. Ricard, and C. Flytzanis, J. Opt. Soc. Am. **B3**, 1647 (1986).
4. L. Genzel, T.P. Martin, and U. Kreibig, Z. Physik **B2**, 339 (1975).
5. G.I. Stegeman and C.T. Seaton, J. Appl. Phys. **58**, 57 (1985).
6. P. Mazzoldi, G.W. Arnold, G. Battaglin, F. Gonella, and R.F. Haglund, Jr., J. Nonlinear Opt. Phys. Mat. **5** (2), 285 (1996) and references therein.
7. A.P. Webb and P.D. Townsend, Phys. D: Appl. Phys. **9**, 1343 (1976).
8. C. Wang, Y. Tao, and S. Wang, J. Non-Cryst. Solids **52**, 589 (1982).
9. I.K. Naik, Appl. Phys. Lett. **43**, 519 (1983).
10. P. Mazzoldi, G.W. Arnold, G. Battaglin, R. Bertoncello, and F. Gonella, Nucl. Instrum. Methods **B91**, 478 (1994) and references therein.
11. G. Battaglin, Nucl. Instrum. Methods **B116**, 102 (1996).
12. R. Bertoncello, A. Glisenti, G. Granozzi, G. Battaglin, F. Caccavale, E. Cattaruzza, and P. Mazzoldi, J. Non-Cryst. Solids **162**, 205 (1993).
13. E. Cattaruzza, G. Mattei, P. Mazzoldi, R. Bertoncello, G. Battaglin, and L. Mirenghi, Appl. Phys. Lett. **67** (19), 2884 (1995).
14. E. Cattaruzza, R. Bertoncello, F. Trivillin, P. Mazzoldi, G. Battaglin, L. Mirenghi, and P. Rotolo, J. Mater. Res. **11**, 229 (1996).
15. P. Mazzoldi, F. Caccavale, E. Cattaruzza, P. Chakraborty, L. Tramontin, A. Boscolo-Boscoletto, R. Bertoncello, F. Trivillin, G. Battaglin, and G.W. Arnold, Nucl. Instrum. Methods **B91**, 505 (1994).
16. R. Bertoncello, F. Trivillin, E. Cattaruzza, P. Mazzoldi, G.W. Arnold, G. Battaglin, and M. Catalano, J. Appl. Phys. **77** (3), 1294 (1995).
17. A.K. Rai and R.S. Bhattacharya, J. Mater. Res. **6**, 2375 (1991).
18. H. Hosono, Phys. Rev. Lett. **74** (1), 110 (1995).
19. R.H. Magruder III, D.H. Osborne, Jr., and R.A. Zuhr, J. Non-Cryst. Solids **176**, 299 (1994).
20. R.H. Magruder III and R.A. Zuhr, J. Appl. Phys. **77** (7), 3546 (1995).
21. K. Fukumi, A. Chayahara, N. Kitamura, T. Akai, J. Hayakawa, K. Fujii, and M. Satou, J. Non-Cryst. Solids **178**, 155 (1994).
22. H. Hosono and R.A. Zuhr, J. Non-Cryst. Solids **178**, 160 (1994).
23. G.S. Was, V. Rotberg, D. Platts, and J. Bomback, Appl. Phys. Lett. **66** (2), 142 (1995).
24. A. Carnera, P. Mazzoldi, A. Boscolo-Boscoletto, F. Caccavale, R. Bertoncello, G. Granozzi, I. Spagnol, and G. Battaglin, J. Non-Cryst. Solids **125**, 293 (1990).
25. P. Mazzoldi, F. Caccavale, E. Cattaruzza, A. Boscolo-Boscoletto, R. Bertoncello, A. Glisenti, G. Battaglin, and C. Gerardi, Nucl. Instrum. Methods **B65**, 367 (1992).
26. T.S. Anderson, R.H. Magruder III, D.L. Kinser, R.A. Zuhr, and D.K. Thomas, Nucl. Instrum. Methods **B124**, 40 (1997) and references therein.
27. J.P. Biersack and L.G. Haggmark, Nucl. Instrum. Methods **174**, 257 (1980).
28. D.A. Shirley, Phys. Rev. **55**, 4709 (1972).
29. J.J. Yeh and I. Lindau, At. Data Nucl. Data Tables **32**, 1 (1985).

Downloaded from https://www.cambridge.org/core. UNIV.STUDI PADOVA-BIBL.RUGGERO, on 05 Mar 2018 at 10:44:56, subject to the Cambridge Core terms of use, available at https://www.cambridge.org/core/terms. https://doi.org/10.1557/JMR.1999.0329

30. M. Antonello, G.W. Arnold, G. Battaglin, R. Bertoncello, E. Cattaruzza, P. Colombo, G. Mattei, P. Mazzoldi, and F. Trivillin, J. Mater. Chem. **8** (2), 457 (1998).
31. J.C. Maxwell-Garnett, Philos, Trans. R. Soc. **203**, 885 (1904).
32. G. Mie, Ann. Physik **25**, 377 (1908).
33. R.H. Doremus, J. Chem. Phys. **42**, 414 (1965) and references therein.
34. G.W. Arnold and J.A. Borders, J. Appl. Phys. **48** (4), 1488 (1977).
35. U. Kreibig and M. Vollmer, in *Optical Properties of Metal Clusters,* edited by U. Gonser, R.M. Osgood, Jr., M.B. Panish, and H. Sakaki (Springer Series in Materials Science, Springer-Verlag, Berlin, Heidelberg, 1995), Vol. 25.
36. J. Neddersen, G. Chumanov, and T.M. Cotton, Appl. Spectrosc. **47**, 1959 (1992).
37. M. Ferrari, L.M. Gratton, A. Maddalena, M. Montagna, and C. Tosello, J. Non-Cryst. Solids **191**, 101 (1995).
38. N. Matsunami and H. Hosono, Appl. Phys. Lett. **63**, 2050 (1993).
39. A. Berger, J. Non-Cryst. Solids **163**, 185 (1993).
40. R. Ruppin, J. Phys. Soc. Jpn. **58**, 1446 (1989).
41. F. Gonella, G. Mattei, P. Mazzoldi, E. Cattaruzza, G.W. Arnold, G. Battaglin, P. Calvelli, R. Polloni, R. Bertoncello, and R.F. Haglund, Jr., Appl. Phys. Lett. **69** (20), 3101 (1996).
42. R.D. Averitt, D. Sarkar, and N.J. Halas, Phys. Rev. Lett. **78**, 4217 (1997).
43. D. Briggs and M.P. Seah, in *Practical Surface Analysis* (J. Wiley & Sons, Chichester, U.K., 1983).
44. *X-ray Photoelectron Spectroscopy Database,* version 1.0 (National Institute of Standards and Technology, Gaithersburg, MD, 1989).
45. J.F. Moulder, W.F. Stickle, P.E. Sobol, and K.D. Bomben, *Handbook of X-ray Photoelectron Spectroscopy,* edited by J. Chastain (Perkin-Elmer Corp., Eden Prairie, MN, 1992).
46. T. Hattori, J. Vac. Sci. Technol. **B11** (4), 1528 (1993).

Downloaded from https://www.cambridge.org/core. UNIV.STUDI PADOVA-BIBL.RUGGERO, on 05 Mar 2018 at 10:44:56, subject to the Cambridge Core terms of use, available at https://www.cambridge.org/core/terms. https://doi.org/10.1557/JMR.1999.0329